Mechanics of Advanced Materials and Structures (2015) **22**, 681–696

ISSN: 1537-6494 print / 1537-6532 online
DOI: 10.1080/15376494.2013.855852

Taylor & Francis
Taylor & Francis Group

A Rate Independent Cohesive Zone Model for Modeling Failure in Quasi-Brittle Materials

NITIN KUMAR[1], AMIRTHAM RAJAGOPAL[1], and MANOJ PANDEY[2]

[1]*Department of Civil Engineering, Indian Institute of Technology, Hyderabad, Andhra Pradesh, India*
[2]*Department of Mechanical Engineering, Indian Institute of Technology, Madras, Tamil Nadu, India*

Received 14 July 2013; accepted 11 October 2013.

Computational modeling of failure in quasi-brittle materials at various length scales is important. In this work we present a rate independent cohesive zone model for modeling failure in quasi-brittle materials. The proposed model can simulate cracking, slipping, and crushing of planes through a traction-separation law. A single surface hyperbolic failure criterion, which naturally comes as a direct extension of Coulomb friction criterion with cut-off in tension and cap-off in compression, has been developed. A Euler backward integration scheme together with a global-local Newton solver compatible with a substepping strategy has been used in numerical computations. The proposed model is then used for modeling of shear wall panels. The numerical results obtained are validated by comparing them with experimental results available in literatures.

Keywords: cohesive zone model, nonlinear fracture, adhesive joints, plasticity, failure criterion, masonry modeling

1. Introduction

Computational modeling of failure in materials and structures has been of interest in the scientific community. The progress has been towards use of concepts from fracture and damage mechanics together with computational tools like finite element, extended finite element, and or mesh free methods for modeling failure. The introductory works on Cohesive Zone Models (CZM) is attributed to [1] and [2]. These are often associated with interface elements for the purpose of modeling crack propagation in various materials, such as metals, polymers, ceramics, and geomaterials. A CZM is characterized by a traction separation law analogous to material constitutive law for a continuum material. This allows to have a fracture process zone ahead of the crack tip defined by two imaginary surfaces and the bulk that localizes the physical fracture. Material outside this zone remains pristine. Once the tractive forces across the two surfaces exceed a certain limit as defined by the traction separation law, the two surfaces start to open and the crack initiates. A zero thickness interface element is used to implement the CZM into a finite element scheme. A comprehensive overview of the different interface elements and their finite element formulation is provided in [3]. Thus, CZM is an explicit expression for fracture state in materials. It represents the relationship of force and displacement. A numeric approach is provided by this model to simulate the behavior of fracture within the crack area.

The quasi-brittle materials have a progressive internal micro crack, even prior to loading the material. Such mechanical behavior is commonly attributed to the heterogeneity of the material, due to the presence of different phases and material defects, like flaws and voids. Initially, these micro cracks are stable, which means that they grow only when the load is increased. Around the peak load an acceleration of crack formation takes place and the formation of macro cracks starts. The macro cracks are unstable, which means that the load has to decrease in order to avoid an uncontrolled growth. Thus, deformation controlled test of such quasi-brittle material results in softening and localization of cracking in a small zone.

Many cohesive models have been formulated and developed in terms of traction separation laws, and are popular for modeling discontinuities in solid mechanics [4]. Cohesive models were originally introduced in the late 1970s to represent rock joints or interfaces in geotechnical models of discontinuous rock masses [5, 6]. Later they were used for fracture analysis of quasi-brittle materials. Hillerborg et al. [7] formulated a fictitious crack cohesive model, with one-dimensional format of tensile de-bonding. It is capable of capturing the loss of cohesion in the fracture process zone. These models were initially used to represent the progressive cracking along straight crack paths in single notched specimens [8], and crack analysis along curvilinear paths in eccentrically notched 3-point bending beams [9]. Later, they were extended to the analysis

Address correspondence to Amirtham Rajagopal, Department of Civil Engineering, Indian Institute of Technology, Ordnance Factory Estate, Medak District, Hyderabad, Andhra Pradesh 502205, India. E-mail: rajagopal@iith.ac.in
Color versions of one or more of the figures in the article can be found online at www.tandfonline.com/umcm.

of multiple crack paths in meso-mechanical studies of concrete or rock materials [10]. The cohesive zone model was also used for the calculation of stress tractions along bi-material interfaces, which is a nontrivial task of extrapolating standard Gauss point stresses in adjacent continuum elements, and the representation of surface tractions along discrete cracks in finite element analysis of LEFM problems requiring systematic re-meshing near the crack tip [11].

The cohesive zone model regard fracture as a gradual phenomenon in which separation takes place across a cohesive zone, and is resisted by cohesive tractions [12]. Thus, cohesive zone elements do not represent any physical material, but describe the cohesive forces which occur when material elements are being pulled apart. Therefore, cohesive zone elements are placed between continuum (bulk) elements. Moreover, cohesive zone models incorporate both strength and energy parameters. They provide a bridge between strength-based models and energy-based models for cracking, slipping, and crushing of material. Several constitutive models have been proposed in the literature for various applications, and with different levels of numerical sophistication.

For geo-mechanics, after the inception proposals in [5] and [13], several plasticity-based cohesive zone models were formulations, such as [14, 15], etc. For the failure modeling of composite like masonry plasticity-based fracture models [16–21] were proposed at micron level. For fracture simulations of concrete elasticity-based cohesive zone models [22], damage-based de-cohesion models [23, 24] and plasticity-based fracture models [25–28] were proposed. Moreover, recent proposals include the rigid plastic simulations [29, 30].

In the present study, a cohesive zone model is formulated in terms of traction separation laws, through plasticity constitutive theory. The cohesive model consists of a single surface hyperbolic yield criterion and comprehends three different failure mechanisms: first, tension cut-off for mode I failure; second, the Coulomb friction model for mode II failure; third, cap for compression failure. Moreover, the model is developed by integrating the differential equation by fully implicit Backward Euler method. These equations are solved by full Newton–Raphson technique in monolithic manner, which lead to combined local/global approach and faster convergence. A careful and detailed investigation has been made to check robustness and accuracy of the algorithm for different load path and nonassociativity. It has been found that sub stepping is required to ensure convergence and accuracy of the final solution at both local and global level. Thus, algorithm is combined with a sub stepping strategy.

This article is structured as follows: After introduction and a brief literature review of cohesive zone models, Section 2 describes the proposed cohesive zone model in terms of classical plasticity, which features fracture energy-based softening of strength parameters. It also emphasizes on the requirement of nonassociated formulation. Section 3 summarizes the algorithmic aspect related to fully implicit integration of the constitutive relations and the Newton–Raphson solution of the local material and the global equilibrium problems, based on a consistent tangent operator. In Section 4, the performance of proposed cohesive zone model is evaluated by loading a cohesive element in direct tension, direct compression, and mixed mode conditions. In Section 5 the single step algorithm is extended to include a sub-stepping strategy to enlarge the range of convergence and improve the accuracy of calculating the internal variables. Section 6 validates the model by numerical modeling of unreinforced masonry shear wall. The shear wall is considered because it shows all the failure mechanisms of cracking, slipping and crushing. Finally, Appendix A summarizes the basic expressions required for the model and the entries for the consistent tangent operators, while Appendix B presents algorithms of local Newton solvers with and without sub-stepping.

2. Cohesive Zone Model

In this section, cohesive model is proposed for failure analysis of quasi-brittle material, which includes potential crack, slip, and crushing of planes. In the following section, a complete description of proposed cohesive zone model is explained in terms of classical plasticity theory.

2.1. *Elastic Behavior*

The 2D constitutive model for cohesive zone model is formulated in terms of one normal and one tangential surface traction, $\boldsymbol{\sigma} = \{\sigma_{nn}, \sigma_{tt}\}^T$, and conjugate relative displacements, $\boldsymbol{\epsilon} = \{u_{nn}, u_{tt}\}^T$. The generalized relation can be written in standard form as:

$$\boldsymbol{\sigma} = \boldsymbol{K}\boldsymbol{\epsilon}, \tag{1}$$

where *nn* and *tt* designate normal and tangential components. Before cracking, slipping, and crushing, the model is assumed to behave elastically, and it is also assumed that normal and traction component are independent of each other. Thus, stiffness can be expressed as:

$$\boldsymbol{K} = diag\{k_{nn}, k_{tt}\}^T. \tag{2}$$

2.2. *Plasticity-Based Cohesive Zone Model*

A rate independent cohesive zone model, defined by hyperbolic function (Eq. 3) has been proposed, see Figure 1. The proposed model is a simple extension of the Coulomb friction criterion with cut-off in tension and cap-off in compression, which results in a single surface yield criteria capable of representing pressure-dependent friction shear failure and cracking by cut-off in-tension and crushing by cap-off in compression under combined normal and tangential stresses. Moreover, the proposed model overcomes the problem of singularity that may occur in multi-surfaces yield criterion:

$$F(\boldsymbol{\sigma}, \boldsymbol{q}) := -[(C - \sigma_{nn}\tan(\phi))]^2 f_c(\boldsymbol{\sigma}, \boldsymbol{q}) f_t(\boldsymbol{\sigma}, \boldsymbol{q}) + \sigma_{tt}^2, \tag{3}$$

$$f_c(\boldsymbol{\sigma}, \boldsymbol{q}) := \frac{2}{\pi}\arctan\left(\frac{\sigma_{nn} - \zeta}{\alpha_c}\right), \tag{4}$$

$$f_t(\boldsymbol{\sigma}, \boldsymbol{q}) := \frac{2}{\pi}\arctan\left(\frac{\xi - \sigma_{nn}}{\alpha_t}\right), \tag{5}$$

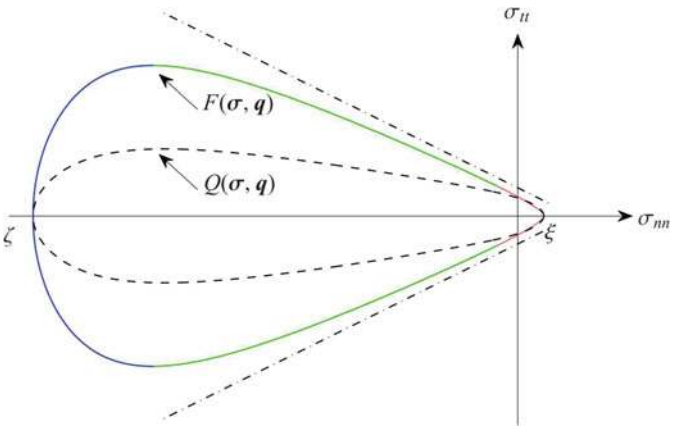

Fig. 1. Trace of failure function $F(\boldsymbol{\sigma}, \boldsymbol{q})$ and potential function $Q(\boldsymbol{\sigma}, \boldsymbol{q})$; solid line represents the tension-cut, shear and compression-cap region with one equation; straight dotted line indicates the Coulomb friction criterion. Note: A transition point from compression cap to Mohr-Coulomb friction criterion, denoted as ζ_c.

where the vector $\boldsymbol{q} = \boldsymbol{q}(C, C_q, \phi, \psi, \xi, \zeta)$ is a function of six internal hardening parameters, which implicate the apparent cohesion (C, C_Q), friction angle (ϕ), dilation angle (ψ), tension strength (ξ), and compression strength (ζ). In the yield function, ξ denotes tension cut-off and ζ denotes compression cap. The functions $f_c(\boldsymbol{\sigma}, \boldsymbol{q})$ and $f_t(\boldsymbol{\sigma}, \boldsymbol{q})$ are the compression cap and tension cut-off functions, respectively. The function $f_c(\boldsymbol{\sigma}, \boldsymbol{q})$ vanishes at the cap and the function $f_t(\boldsymbol{\sigma}, \boldsymbol{q})$ vanishes at tension-cut. For all other stress-states both functions have a value approximately equal to one. The parameters α_c and α_t control the curvature of the compression cap and tension cut-off at transition region.

Moreover, if f_t and f_c fixed to 1, the present single yield surface criterion reduce to Mohr–Coulomb criterion. Additionally, if $\phi = 0$, it further reduces to the Tresca criterion. On the other hand, if only ϕ is fixed 0 then failure surface of present yield criterion becomes rectangular with different yield value for compression, tension and shear.

Generally, a nonassociated formulation is used to characterize the frictional behavior of quasi-brittle material, such as concrete, ceramics, etc., which exhibits the significant pressure-sensitivity. The frictional material exhibits the phenomenon of dilatancy due to irregularity of surface in sliding, which tends to separate and open the two faces under relative tangential displacements. It is widely accepted that the dilatancy diminishes with the increase in level of compression, and finally disappears at very high levels of compression [31, 32]. In addition, the dilatancy decreases as sliding progresses [33, 34]. Therefore, due to different dependence of strength and dilatancy on normal stress leads to the requirement of a nonassociated formulation. The plastic potential is described in terms of another hyperbolic function with different values of apparent cohesion (C_Q) and frictional angle (dilation angle (ψ)), with the same tensile (ξ) and compressive strength (ζ). The expression of potential function reads:

$$Q(\boldsymbol{\sigma}, \boldsymbol{q}) := -[C_Q - \sigma_{nn} \tan(\psi)]^2 f_c(\boldsymbol{\sigma}, \boldsymbol{q}) f_t(\boldsymbol{\sigma}, \boldsymbol{q}) + \sigma_{tt}^2. \quad (6)$$

2.3. *Evolution Laws*

Evolution laws for hardening or softening behavior for the cohesive zone model is defined by the rate of plastic work per unit volume. In the present study, the evolution of yield surface has been assumed such that, during plastic loading in tension-shear region, tensile strength (ξ) decreases exponentially while friction angle (ϕ) remains unchanged, and in the compression-shear region both friction and tensile strength degrade exponentially (Figure 2a). In addition, the compression strength changes when plastic loading path intersects with the compression cap (Figure 2b). The above assumptions can be implemented by using four internal variables, i.e., $\dot{\boldsymbol{W}}^p := \dot{\boldsymbol{W}}^p(\dot{w}_1^p, \dot{w}_2^p, \dot{w}_3^p, \dot{w}_4^p)$, where $\dot{w}_1^p$ and $\dot{w}_2^p$ represent degradation in tensile strength, $\dot{w}_2^p$ and $\dot{w}_3^p$ govern the frictional strength degradation, and $\dot{w}_4^p$ gives change in the compression strength (see figure):

$$\dot{w}_1^p := \langle \sigma_{nn} \rangle \dot{u}_{nn}^p, \quad (7)$$

$$\dot{w}_2^p := (\sigma_{tt} - \sigma_{tt_{r1}} sign(\sigma_{tt})) \dot{u}_{tt}^p, \quad (8)$$

$$\dot{w}_3^p := (\sigma_{tt_{r1}} - \sigma_{tt_{r2}}) sign(\sigma_{tt}) \dot{u}_{tt}^p, \quad (9)$$

$$\dot{w}_4^p := \langle \langle \sigma_{nn} \rangle \rangle \dot{u}_{nn}^p \quad for\ \sigma_{nn} < \zeta_c, \quad (10)$$

where the symbol $\langle\rangle$ denotes for Macaulay bracket and $\langle x \rangle = (x + |x|)/2$ and $\langle\langle x \rangle\rangle = (x - |x|)/2$. $\dot{u}_{nn}^p$ and $\dot{u}_{tt}^p$ is normal and tangential relative plastic displacements. ζ_c denotes the transition point from compression cap to Mohr–Coulomb

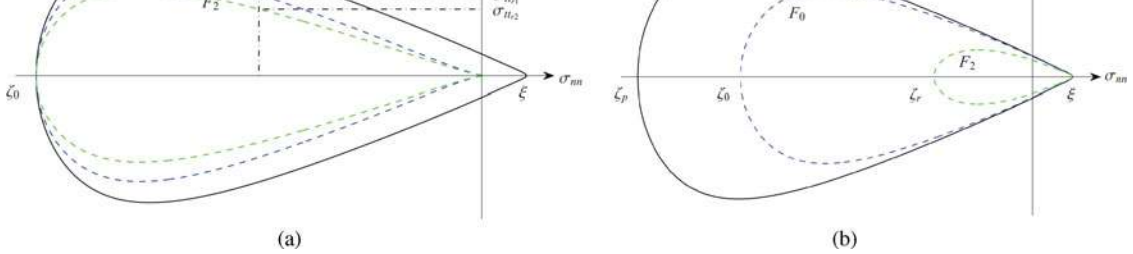

Fig. 2. Evolution of yield surfaces: (a) tension shear region; (b) compression region.

friction envelope (see Figure 1, a point between red and green line). $\sigma_{tt_{r1}}$ is the tangential strength when tensile strength is completely exhausted; $\sigma_{tt_{r2}}$ is minimum tangential strength for the final contracted yield surface, see Figure 2a. In tension-shear region, $\sigma_{tt_{r1}}$ and $\sigma_{tt_{r2}}$ are assumed to be zero and in compression-shear region they can be expressed as:

$$\sigma^2_{tt_{r1}} = -2C_r \tan\phi \; f_c f_t, \tag{11}$$

$$\sigma^2_{tt_{r2}} = -2C_r \tan\psi_r \; f_c f_t. \tag{12}$$

The hardening parameter $\boldsymbol{q}$ can be related to the internal variables as follows:

$$C := C_r + (C_0 - C_r)\exp^{-\beta_C\left(\frac{w_1^p}{G_f^I} + \frac{w_2^p}{G_f^{II}}\right)}, \tag{13}$$

$$C_Q := C_{Q_r} + (C_{Q_0} - C_{Q_r})\exp^{-\beta_{C_Q}\left(\frac{w_1^p}{G_f^I} + \frac{w_2^p}{G_f^{II}}\right)}, \tag{14}$$

$$\phi := \phi_r + (\phi_0 - \phi_r)\exp^{-\beta_\phi w_3^p}, \tag{15}$$

$$\psi := \psi_r + (\psi_0 - \psi_r)\exp^{-\beta_\psi w_3^p}, \tag{16}$$

$$\xi := \xi_0 \exp^{-\beta_\xi\left(\frac{w_1^p}{G_f^I} + \frac{w_2^p}{G_f^{II}}\right)}, \tag{17}$$

$$\zeta = \begin{cases} \zeta_0 + (\zeta_p - \zeta_0)\sqrt{\left(\frac{2w_4^p}{w_p}\right) - \left(\frac{w_4^p}{w_p}\right)^2} & \text{if } w_4^p \le w_p \\ \zeta_0 + (\zeta_p - \zeta_p)\left(\frac{w_4^p - w_p}{w_m - w_p}\right)^2 & \text{if } w_p \le w_4^p \le w_m, \\ \zeta_r + (\zeta_m - \zeta_r)\exp^{\beta_\zeta\left(\frac{w_4^p - w_p}{\zeta_m - \zeta_r}\right)} & \text{if } w_4^p > w_m \end{cases} \tag{18}$$

where G_f^I and G_f^{II} are the mode I and mode II fracture energy and β_i is a parameter that controls the softening of the internal variable. The subscript 0 stands for initial value and r for residual value whereas subscript p and m indicate intermediate values. The preceding hardening equation can be written in a compact form as follows:

$$\dot{\boldsymbol{W}}^p = \boldsymbol{H}\dot{\boldsymbol{\epsilon}}^p. \tag{19}$$

2.4. *Elasto-Plastic Tangent Operator*

In accordance with the theory of plasticity, the relative displacement can be decomposed into an elastic part and a plastic part:

$$\boldsymbol{\epsilon} = \boldsymbol{\epsilon}^e + \boldsymbol{\epsilon}^p, \tag{20}$$

where $\boldsymbol{\epsilon}^e$ and $\boldsymbol{\epsilon}^p$ are the elastic displacement and plastic or irreversible displacement respectively and the notion of irreversibility of plastic flow can be introduced by nonassociated flow rule. It can be written in rate form as:

$$\dot{\boldsymbol{\epsilon}}^p = \dot{\lambda}\boldsymbol{m}, \tag{21}$$

where $\dot{\lambda}$ is the constant slip rate or plastic multiplier. The plastic multiplier can be found by checking the consistency condition (persistency condition) together with Kuhn–Tucker condition ($F \le 0, \dot{\lambda} \ge 0, \dot{\lambda}F = 0$). The consistency condition can be written as $\dot{\lambda}\dot{F} = 0$ for yield condition $\dot{\lambda} > 0$ and $\dot{F} = 0$ and we can be written as:

$$\dot{F} = \frac{\partial F}{\partial \boldsymbol{\sigma}}\dot{\boldsymbol{\sigma}} + \frac{\partial F}{\partial \boldsymbol{q}}\dot{\boldsymbol{q}} = 0, \tag{22}$$

$$\dot{\lambda} = \frac{\boldsymbol{n}\boldsymbol{K}\boldsymbol{\epsilon}}{\boldsymbol{n}^T\boldsymbol{K}\boldsymbol{m} + \boldsymbol{p}^T\boldsymbol{\varpi}}, \tag{23}$$

in which $\boldsymbol{m} := \partial Q/\partial\boldsymbol{\sigma}$, $\boldsymbol{n} := \partial F/\partial\boldsymbol{\sigma}$, $\boldsymbol{p} := \partial Q/\partial\lambda$, and $\boldsymbol{\varpi} := (\partial\boldsymbol{q}/\partial\boldsymbol{W}^p)(\partial\boldsymbol{W}^p/\partial\boldsymbol{\epsilon}^p)(\partial\boldsymbol{\epsilon}^p/\partial\lambda) = (\partial\boldsymbol{q}/\partial\boldsymbol{W}^p)\boldsymbol{H}\boldsymbol{m}$. We can define hardening parameter in its rate form as $\boldsymbol{q} = \dot{\lambda}\boldsymbol{\varpi}$. Putting the plastic multiplier ($\dot{\lambda}$) in the rate form of stress relationship to get elasto-plastic tangent modulus $\boldsymbol{K}^{ep}$, i.e.,

$$\dot{\boldsymbol{\sigma}} = \boldsymbol{K}(\dot{\boldsymbol{\epsilon}} - \dot{\lambda}\boldsymbol{m}) = \boldsymbol{K}^{ep}\dot{\boldsymbol{\epsilon}}, \tag{24}$$

$$\boldsymbol{K}^{ep} = \boldsymbol{K} - \frac{\boldsymbol{K}\boldsymbol{m}\otimes\boldsymbol{n}\boldsymbol{K}}{\boldsymbol{n}^T\boldsymbol{K}\boldsymbol{m} + \boldsymbol{p}^T\boldsymbol{\varpi}}. \tag{25}$$

3. Algorithmic Aspect

In the present section, the cohesive zone model is implemented into a finite element framework, which gives rise to a set of nonlinear algebraic-differential equations, and they are integrated by Backward Euler method. The Newton–Raphson scheme is used to solve nonlinear system of equations, which leads to combined local and global approach. Local solver provides the new internal state variable for a given relative displacement, subsequently global solver provides the solution for the unbalanced force to accommodate stress distribution within the finite load increments.

3.1. *Elastic Predictor-Plastic Correct Strategy*

The backward Euler method is a first-order (i.e., local truncation error is $O(h^2)$ for a single step) method and is unconditionally stable. The integration procedure leads to a set of

Table 1. Elastic material property for the brick and joints

Brick		Joint	
E, N/mm^2	ν	K_{nn}, N/mm^3	K_{tt}, N/mm^3
2000	0.15	1000	1000

Table 2. Inelastic material property for the joints

Tension		Shear					Cap
ξ_0, N/mm^2	G_f^I, Nmm/mm^2	$C_0 \setminus C_r$, N/mm^2	$C_{Q0} \setminus C_{Qr}$, N/mm^2	$\phi_0 \setminus \phi_r$, radian	ψ, radian	G_f^{II}, Nmm/mm^2	ζ_p, N/mm^2
2.0	$5\xi_0^2/2K_{nn}$	$1.4\xi_0/0.1C_Q$	$1.1\xi_0/0.1C_Q$	0.65/0.50	0.30/0.20	$10G_f^I$	30

algebraic-incremental equations, which can be split into a elastic predictor, followed by plastic corrector if and only if the trial stress-state violates the current yield condition.

The time discretization of an interval of interest as $[0,\ T] = \bigcup_{n=1}^{N}[t_n,\ t_{n+1}]$. The relevant problem can be seen with in time interval $[t_n,\ t_{n+1}]$. It is assumed that the stress-state $(\boldsymbol{\sigma}_n, \boldsymbol{q}_n)$ at current time $t = t_n$ should satisfy the equilibrium conditions and be admissible. For prescribed increment in relative displacement $\dot{\boldsymbol{\epsilon}}$, at the next time step $t_{n+1} = t_n + \Delta t$ the relative displacement is given by $\boldsymbol{\epsilon}_{n+1} = \boldsymbol{\epsilon}_n + \Delta\boldsymbol{\epsilon}$, and this can be split into two parts, i.e., $\Delta\boldsymbol{\epsilon} = \Delta\boldsymbol{\epsilon}^e + \Delta\boldsymbol{\epsilon}^p$. According to the elastic predictor-plastic corrector strategy, the stress and internal variables can be written in their incremental form as:

$$\boldsymbol{\sigma}_{n+1} = \boldsymbol{\sigma}_n + \boldsymbol{K}\Delta\boldsymbol{\epsilon}^e = \boldsymbol{\sigma}_n + \boldsymbol{K}(\Delta\boldsymbol{\epsilon} - \Delta\boldsymbol{\epsilon}^p), \tag{26}$$

$$\boldsymbol{\sigma}_{n+1} = \boldsymbol{\sigma}_{n+1}^{trial} + \Delta\lambda_{n+1}\boldsymbol{K}\boldsymbol{m}_{n+1}, \tag{27}$$

$$\boldsymbol{q}_{n+1} = \boldsymbol{q}_n + \Delta\lambda_{n+1}\boldsymbol{\varpi}_{n+1}, \tag{28}$$

$$F(\boldsymbol{\sigma}_{n+1}, \boldsymbol{q}_{n+1}) = 0, \tag{29}$$

where $\boldsymbol{\sigma}_{n+1}^{trial} = \boldsymbol{\sigma}_n + \boldsymbol{K}\Delta\boldsymbol{\epsilon}$ is the trial stress. The backward Euler method gives rise to nonlinear system of equations, which has to be solved to get actual stress state. In the present study, full Newton–Raphson method is used to solve nonlinear system of equations. It provides quadratic convergence when the initial root is sufficiently close to the converged solution, and also ensures the asymptotic quadratic convergence at the global level for structural equilibrium. Newton–Raphson strategy is used for the solution of non-linear equation in monolithic format, as illustrated in [35–37] for the J_2 plasticity. The strategy is highly influenced by the choice of the independent variables and sequence of the numerical operations. It requires the determination of residual for the set non-linear Eqs. (27), (28), and (29). It can be written as:

$$\boldsymbol{r}(\boldsymbol{\sigma}_{n+1}, \boldsymbol{q}_{n+1}, \Delta\lambda_{n+1}) = \begin{cases} \boldsymbol{\sigma}_{n+1} - \boldsymbol{\sigma}_{n+1}^{trial} + \Delta\lambda_{n+1}\boldsymbol{K}\boldsymbol{m}_{n+1} = 0 \\ \boldsymbol{q}_{n+1} - \boldsymbol{q}_n + \Delta\lambda_{n+1}\boldsymbol{\varpi}_{n+1} = 0 \\ F(\boldsymbol{\sigma}_{n+1}, \boldsymbol{q}_{n+1}) = 0 \end{cases}. \tag{30}$$

After linearizing the residual and then expanding it, we can write:

$$\boldsymbol{r}(\boldsymbol{\sigma} + \delta\boldsymbol{\sigma}, \boldsymbol{q} + \delta\boldsymbol{q}, \Delta\lambda + \delta\lambda) = \boldsymbol{r}(\boldsymbol{\sigma}, \boldsymbol{q}, \Delta\lambda) + \frac{\boldsymbol{r}(\boldsymbol{\sigma}, \boldsymbol{q}, \Delta\lambda)}{\partial(\boldsymbol{\sigma}, \boldsymbol{q}, \lambda)} \begin{bmatrix} \delta\boldsymbol{\sigma} \\ \delta\boldsymbol{q} \\ \delta\lambda \end{bmatrix} + O(\delta^2), \tag{31}$$

where the truncation is performed after the first-order terms ($O(\delta^2) \cong 0$) and $\frac{\boldsymbol{r}(\boldsymbol{\sigma}, \boldsymbol{q}, \Delta\lambda)}{\partial(\boldsymbol{\sigma}, \boldsymbol{q}, \lambda)}$ is the gradient of residual with respect to its variables, i.e., $\boldsymbol{\sigma}$, $\boldsymbol{q}$, λ commonly known as Jacobian. The Jacobian for residual at time step $n + 1$ can be

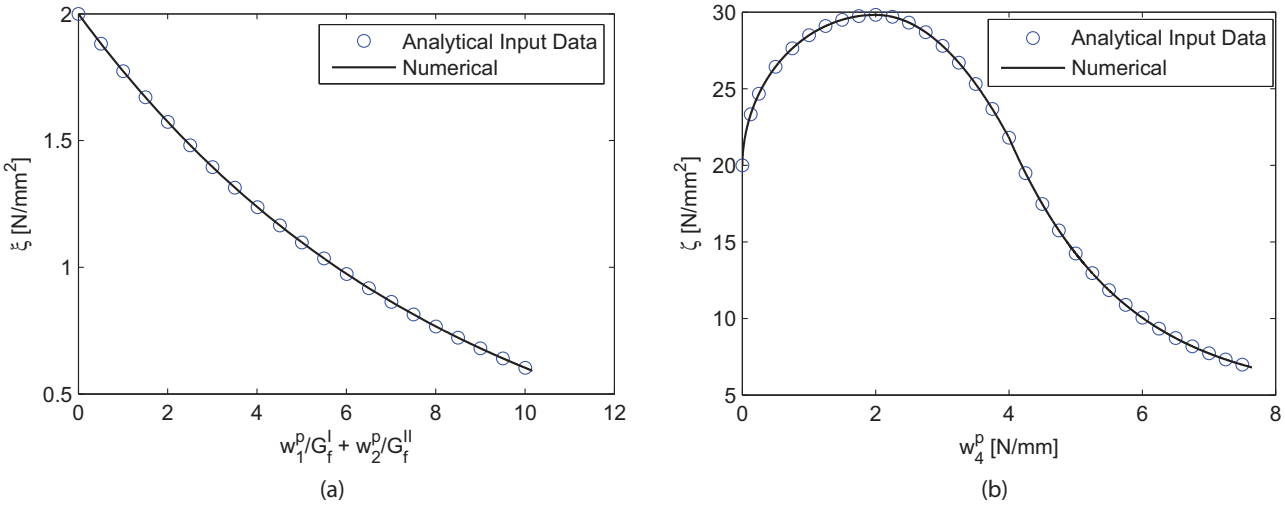

Fig. 3. Plot of verification example: (a) direct tension test; (b) direct compression test.

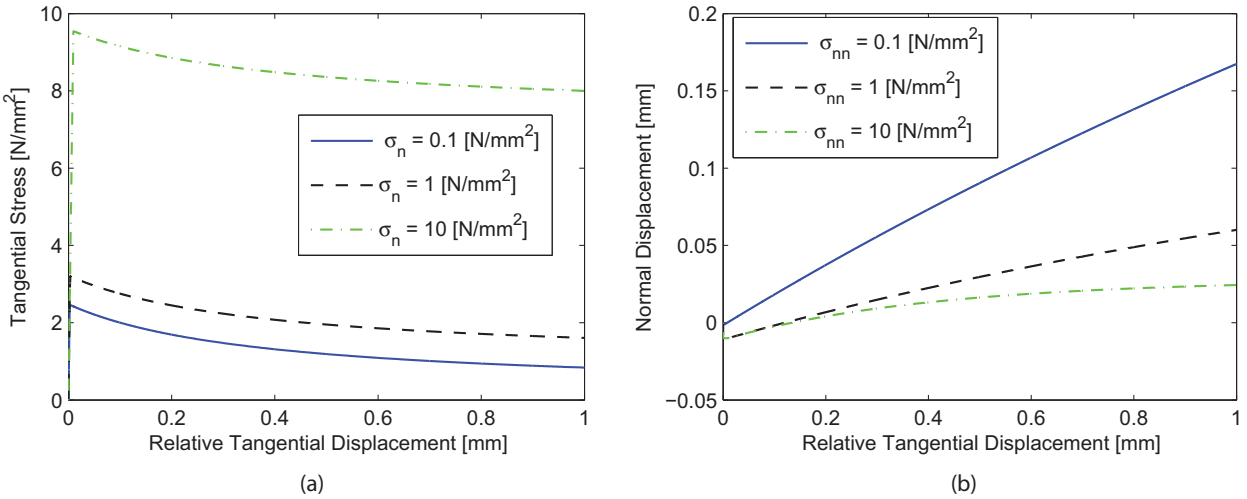

Fig. 4. Plot of verification example under direct shear test under different compressive stress.

expressed as:

$$\boldsymbol{J}(\boldsymbol{\sigma}_{n+1}, \boldsymbol{q}_{n+1}, \Delta\lambda_{n+1}) = \begin{bmatrix} \boldsymbol{I} + \Delta\lambda \boldsymbol{K} \dfrac{\partial \boldsymbol{m}}{\partial \boldsymbol{\sigma}} & \Delta\lambda \boldsymbol{K} \dfrac{\partial \boldsymbol{m}}{\partial \boldsymbol{q}} & \boldsymbol{K}\boldsymbol{m} \\ -\Delta\lambda \boldsymbol{K} \dfrac{\partial \boldsymbol{\varpi}}{\partial \boldsymbol{\sigma}} & -\Delta\lambda \boldsymbol{K} \dfrac{\partial \boldsymbol{\varpi}}{\partial \boldsymbol{q}} & -\boldsymbol{\varpi} \\ \dfrac{\partial \boldsymbol{F}}{\partial \boldsymbol{\sigma}} & \dfrac{\partial \boldsymbol{F}}{\partial \boldsymbol{q}} & 0 \end{bmatrix}. \quad (32)$$

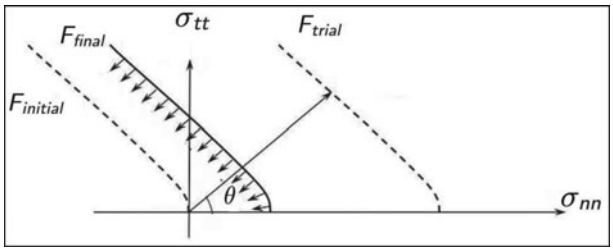

Fig. 5. Plot of the initial yield surface $F_{initial}$; plot of the yield surface at trial stress F_{trial}; plot of the shrunk or final yield surface F_{final}.

The actual solution is achieved by letting the residual go to zero for that current time step during plastic loading. This can be achieved by performing local iteration cycles. The iterations will end when residual becomes smaller than a prescribed tolerance value:

$$0 = \boldsymbol{r}(\boldsymbol{\sigma}^k_{n+1}, \boldsymbol{q}^k_{n+1}, \Delta\lambda^k_{n+1}) + \boldsymbol{J}^{-1}(\boldsymbol{\sigma}^k_{n+1}, \boldsymbol{q}^k_{n+1}, \Delta\lambda^k_{n+1}) \begin{bmatrix} \delta\boldsymbol{\sigma}^{k+1}_{n+1} \\ \delta\boldsymbol{q}^{k+1}_{n+1} \\ \delta\lambda^{k+1}_{n+1} \end{bmatrix}, \quad (33)$$

$$\begin{bmatrix} \delta\boldsymbol{\sigma}^{k+1}_{n+1} \\ \delta\boldsymbol{q}^{k+1}_{n+1} \\ \delta\lambda^{k+1}_{n+1} \end{bmatrix} = -\boldsymbol{J}^{-1}(\boldsymbol{\sigma}^k_{n+1}, \boldsymbol{q}^k_{n+1}, \Delta\lambda^k_{n+1}) \times \boldsymbol{r}(\boldsymbol{\sigma}^k_{n+1}, \boldsymbol{q}^k_{n+1}, \Delta\lambda^k_{n+1}), \quad (34)$$

Table 3. Convergence of algorithm without sub-stepping for different load path, at a Gauss point level

	Tension-shear region						
	$\theta = 0$	$\theta = 15$	$\theta = 30$	$\theta = 45$	$\theta = 60$	$\theta = 75$	$\theta = 90$
$N = 5$	4	8	7	6	7	6	6
$N = 25$	5	16	14	12	14	8	8
$N = 125$	5	Fail	14	15	16	8	10
$N = 625$	6	Fail	Fail	Fail	Fail	Fail	12
	Compression-shear region						
	$\theta = 90$	$\theta = 105$	$\theta = 120$	$\theta = 135$	$\theta = 150$	$\theta = 175$	$\theta = 180$
$N = 5$	6	6	8	8	11	25	*E*
$N = 25$	8	16	12	13	12	12	4
$N = 125$	10	20	13	Fail	13	12	7
$N = 625$	12	22	17	Fail	17	16	9

Table 4. Convergence of algorithm with sub-stepping for different load path, at a Gauss point level

Tension-shear region							
	$\theta = 0$	$\theta = 15$	$\theta = 30$	$\theta = 45$	$\theta = 60$	$\theta = 75$	$\theta = 90$
$N = 5$	4	8	7	6	7	6	6
$N = 25$	5	16	14	12	14	8	8
$N = 125$	5	39(2)	14	15	16	8	10
$N = 625$	6	198(8)	113(8)	101(8)	117(8)	64(8)	12
Compression-shear region							
	$\theta = 90$	$\theta = 105$	$\theta = 120$	$\theta = 135$	$\theta = 150$	$\theta = 175$	$\theta = 180$
$N = 5$	6	6	8	8	11	25	E
$N = 25$	8	16	12	13	12	12	4
$N = 125$	10	20	13	97(8)	13	12	7
$N = 625$	12	22	17	481(40)	17	16	9

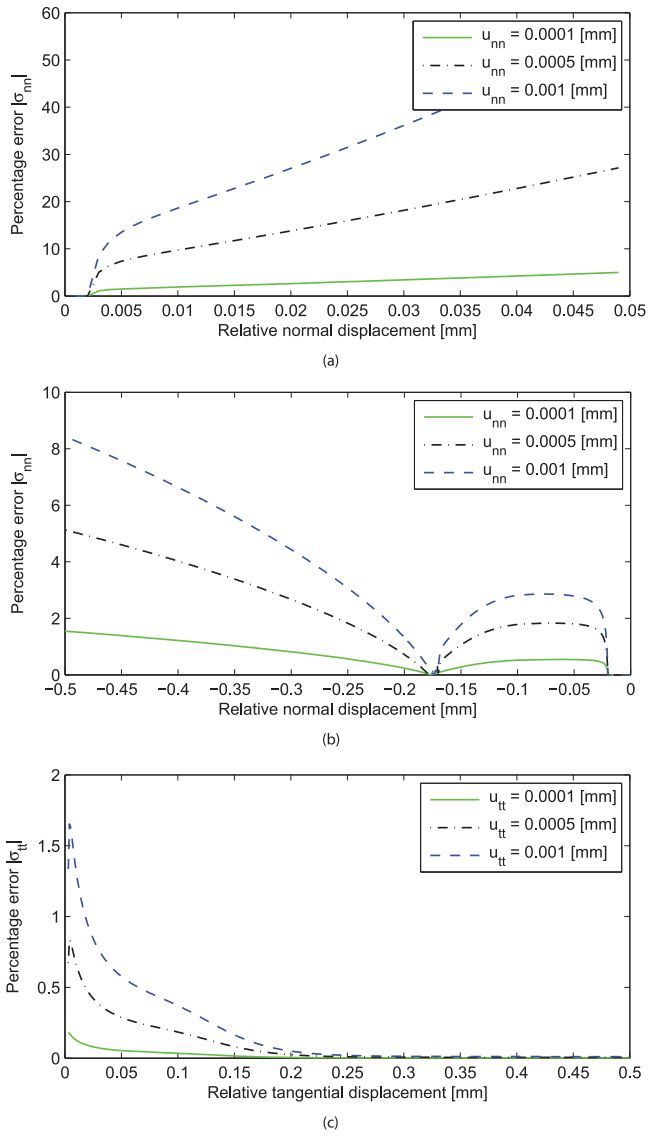

Fig. 6. Plot for error stress response along entire loading path: (a) tension; (b) compression; (c) shear.

$$\begin{bmatrix} \boldsymbol{\sigma}_{n+1}^{k+1} \\ \boldsymbol{q}_{n+1}^{k+1} \\ \lambda_{n+1}^{k+1} \end{bmatrix} = \begin{bmatrix} \boldsymbol{\sigma}_{n+1}^{k} \\ \boldsymbol{q}_{n+1}^{k} \\ \lambda_{n+1}^{k} \end{bmatrix} + \begin{bmatrix} \delta\boldsymbol{\sigma}_{n+1}^{k+1} \\ \delta\boldsymbol{q}_{n+1}^{k+1} \\ \delta\lambda_{n+1}^{k+1} \end{bmatrix}. \tag{35}$$

3.2. *Consistent Tangent Operator*

The converged solution form local Newton–Raphson iteration can be used for the determination of consistent tangent operator $\frac{\Delta\boldsymbol{\sigma}}{\Delta\boldsymbol{\epsilon}}$ for the current time step. Thus, in order to compute the tangent operator using the Jacobian, we have to differentiate the residual with respect to the relative displacement and then by using the chain rule, finally we will get:

$$\begin{bmatrix} \left[\frac{\partial\boldsymbol{\sigma}}{\partial\boldsymbol{\epsilon}}\right]_{2x2} \\ \left[\frac{\partial\boldsymbol{q}}{\partial\boldsymbol{\epsilon}}\right]_{6x2} \\ \left[\frac{\partial\lambda}{\partial\boldsymbol{\epsilon}}\right]_{1x2} \end{bmatrix}_{9x2} = \boldsymbol{J}^{-1}(\boldsymbol{\sigma}_{n+1}, \boldsymbol{q}_{n+1}, \Delta\lambda_{n+1})_{9x9} \begin{bmatrix} \boldsymbol{K} \\ 0 \\ 0 \end{bmatrix}_{9x2} \tag{36}$$

The consistent tangent operator can extracted from the preceding expression, and we can define the consistent tangent

Table 5. Convergence of algorithm without sub-stepping for different dilatency for load step = 0.005, at a Gauss point level

	$p = 0$	$p = 0.1$	$p = 1$	$p = 10$	$p = 20$	$p = 22$
$\psi = 0$	3	3	3	3	13	16
$\psi = 15$	7	7	7	8	24	16
$\psi = 30$	8	8	9	18	39	Fail
$\psi = 45$	10	10	11	Fail	Fail	Fail
$\psi = 60$	13	13	17	Fail	Fail	Fail
$\psi = 75$	41	67	83	Fail	Fail	Fail
$\psi = 90$	Fail	Fail	Fail	Fail	Fail	Fail

Table 6. Convergence of algorithm without sub-stepping for different dilatency for load step = 0.00001, at a Gauss point level

	$p = 0$	$p = 0.1$	$p = 1$	$p = 10$	$p = 20$	$p = 22$
$\psi = 0$	2	2	2	3	3	15
$\psi = 15$	2	2	2	3	3	15
$\psi = 30$	2	2	2	3	4	16
$\psi = 45$	2	2	3	3	4	16
$\psi = 60$	3	3	3	3	4	16
$\psi = 75$	4	4	4	6	6	25
$\psi = 90$	4	4	9	11	17	27

operator as:

$$\left[\frac{\partial \boldsymbol{\sigma}}{\partial \boldsymbol{\epsilon}}\right]_{2x2} = O_{2x2}\left\{\boldsymbol{J}^{-1}(\boldsymbol{\sigma}_{n+1}, \boldsymbol{q}_{n+1}, \Delta\lambda_{n+1})_{9x9}\begin{bmatrix}\boldsymbol{K}\\0\\0\end{bmatrix}_{9x2}\right\}. \quad (37)$$

4. Verification of Cohesive Zone Model at the Constitutive Level

The formulated constitutive model for the cohesive zone is verified by implementing a single zero-thickness interface element, which is a 4-node 2D cohesive element with two integration points. The verification examples include interface in tension, compression, and shear mode condition. The implementation is done in ABAQUS [38], by using the user defined subroutine UMAT, which allows the definition of a user defined mechanical constitutive model for a material. The material parameters used for verification are tabulated in Tables 1 and 2, while the missing parameters are obtained indirectly from the calibration process. Specifically, to find the values of mode I and mode II fracture energy, it is assumed that $G_f^I = 5G_{f\min}^I$ and $G_f^{II} = 10G_f^I$, where $G_{f\min}^I = \xi_0^2/2k_{nn}$ corresponding to the perfectly brittle tensile fracture.

The model is verified by using basic numerical example, i.e., tension, compression, and shear. It can be observed from Figures 3a and 3b, that the internal hardening variable coincides well with the analytical values obtained from Eqs. (17) and (18). Figure 4a shows distribution of tangential stress with relative tangential displacement plotted for different compressive stress (0.1, 1, 10 Mpa). A shear softening behavior is observed. The result shows that the shear capacity of the interface increases with an increase in compressive stress. After the initial elastic response, all response curves show a similar post-peak behavior, with a steeper part given by the decrease of all softening parameters ($\boldsymbol{q}$). After that, ξ remains zero, and the shear traction diminishes. Finally, all softening curves tend to the residual shear value that corresponds to the residual cohesion (C_r) and friction angle (ϕ_r).

In Figure 4b, the distribution of normal displacements with relative tangential displacements is plotted. It can be observed that the dilatancy decreases with increase in compressive stress, and approaches a limiting value when the interface degrades to the residual dilation angle (ψ_r).

5. Sub Stepping

The robustness, accuracy, and nonassociative nature of the present numerical algorithm are tested. A parameter study has been performed to check these aspects on the proposed cohesive zone model and the numerical implementation of different examples are presented below.

5.1. *Robustness*

To check the robustness of proposed algorithm, a set of different load paths, and different load increments are applied to the model. Seven load paths have been considered each for tension shear and compression regions respectively. Load has been applied in all cases from $\sigma = 0$ up to a certain value of the trial stress state, σ^{trail}. In particular, four load increments are considered, namely, $N = 5, 25, 125, 625$ (see Figure 5). The material parameters used in these examples are given in Tables 1 and 2. The results of these numerical examples are given in Table 3, in terms of number of iterations required for the convergence of algorithm with the tolerance of $1e^{-10}$.

The result shows that for load paths whose directions are different from $\theta = 0$ and $\theta = 90$, the algorithm does not converge if the loading step size is larger than 125. It demonstrates the need for sub stepping to achieve optimal performance. The sub stepping procedure will only take place when the algorithm does not reach convergence within a prescribed number of iterations. To check the results of this new procedure the same set of numerical tests are repeated, and the results obtained are given in Table 4. The number of iterations is augmented

Table 7. Convergence of algorithm with sub-stepping for different dilatency for load step = 0.005, at a Gauss point level

	$p = 0$	$p = 0.1$	$p = 1$	$p = 10$	$p = 20$	$p = 22$
$\psi = 0$	3	3	3	3	13	16
$\psi = 15$	7	7	7	8	24	16
$P = 30$	8	8	9	18	39	59(6)
$\psi = 45$	10	10	11	39(3)	66(3)	66(3)
$\psi = 60$	13	13	17	116(9)	178(6)	220(5)
$\psi = 75$	21(2)	25(3)	75(10)	121(3)	138(26)	539(26)
$\psi = 90$	37(9)	41(9)	57(9)	390(75)	341(57)	942(57)

Table 8. Properties for potential brick cracks

Elastic		Inelastic	
K_{nn}, N/mm^3	K_{tt}, N/mm^3	ξ_0, N/mm^2	G_f^I, Nmm/mm^2
10^6	10^6	2.0	0.08

Table 9. Elastic material property for the brick and joints

Brick		Joint	
E, N/mm^2	ν,	K_{nn}, N/mm^3	K_{tt}, N/mm^3
16700	0.15	82; 110; 82	36; 50; 36

by the total number of sub increments between parentheses, which are required for convergence.

5.2. *Accuracy*

It has also been observed that the number of iterations increases as the load step size increases. However, there are special situations in which they do not follow this trend, i.e., uniaxial tension ($\theta = 0$), pure shear ($\theta = 90$), and uniaxial compression ($\theta = 180$). If the convergence for some special situation does not depend on the loading step size, the issue remains whether the accuracy of the solution depends strongly on the load step size. To determine these aspects, three different load steps are considered where u equals 1×10^{-4}, 5×10^{-4}, and 1×10^{-3}. A fourth loading size step with u equals 1×10^{-5} is used to compare the accuracy of the results. This step size is considered sufficiently small to serve as an accurate reference solution for making the comparison and estimating the error.

The results are plotted in Figure 6, which shows that:

- the error in the solution increases as the load step size increases;
- the integration algorithm requires sub stepping not only to ensure convergence of the solution but also to ensure the accuracy of the final solution. This is evident from the fact that a decrease in percentage error of stress is observed with a decrease in load step.

5.2.1. *Nonassociativity*

The capacity of proposed algorithm for different nonassociativity is checked here. A set of different dilatancy angles for a given load step is applied to 2D cohesive model. Seven dilatancy angles are considered $\psi = 0,\ 15,\ 30,\ 45,\ 60,\ 75,\ 90$. The displacement is applied in tangential direction at different vertical pressures, i.e., $p = 0,\ 0.1,\ 1,\ 10,\ 20,\ 22$. The result of these numerical examples are summarized in Tables 5 and 6, in terms of the number of iterations required for the convergence of algorithm with the tolerance of $1e^{-10}$.

The results show that for higher dilatancy angles and load steps, the algorithm does not converge. Thus, sub stepping is also required for robust nonassociativity. The same set of numerical tests is repeated for the algorithm with sub stepping, and the results are summarized in Table 7. The number of iterations is augmented by the total number of sub increments between parentheses, which are required for convergence.

5.2.2. *Algorithm Aspect with Sub Stepping*

The algorithm requires sub stepping not only to ensure convergence of the solution but also to ensure the accuracy of the final solution at both local and global level. Fortunately, it is possible to integrate the constitutive equations by sub-dividing the load at the constitutive level [39–41]. Based on these considerations, a sub-stepping scheme has been developed for the present cohesive model. This technique starts with the previous system of Eq. (30). The algebraic problem is modified significantly in order to obtain consistent tangent operator in the case of sub stepping. It is assumed that any increment can be subdivided into N sub-increments, which could be of different sizes but the sum of all sub-increments always equals to the total displacement at the end of the increment:

$$\Delta\epsilon = \sum_{i=0}^{N} \Delta\epsilon^i = \Delta\epsilon\left(\eta^i\right), \tag{38}$$

$$\text{where } 0 < \eta^i < 1 \text{ and } \sum_{i=0}^{N} \eta^i = 1.$$

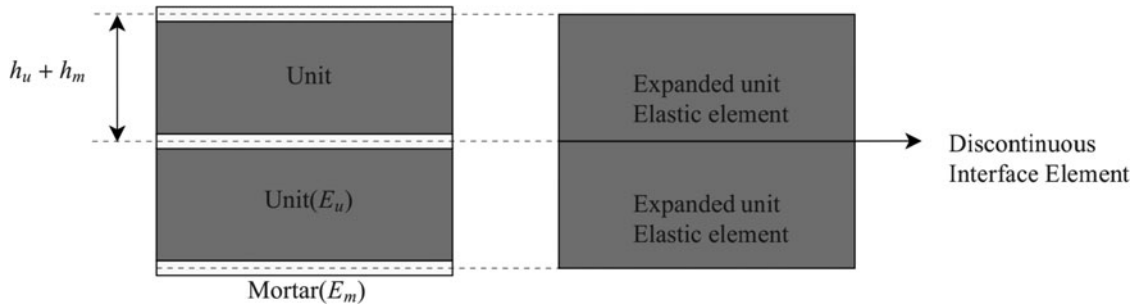

Fig. 7. Simplified micro-modeling.

Table 10. Inelastic material property for the joints

Tension		Shear					Cap
ξ_0, N/mm^2	G_f^I, Nmm/mm^2	$C_0 \setminus C_r$, N/mm^2	$C_{Q0} \setminus C_{Qr}$, N/mm^2	$\phi_0 \setminus \phi_r$, radian	ψ, radian	G_f^{II}, Nmm/mm^2	ζ_p, N/mm^2
0.25	$5\xi_0^2/2K_{nn}$	$1.4\xi_0/0.1C_Q$	$1.1\xi_0/0.1C_Q$	0.65/0.50	0	$10G_f^I$	10.5

Hence, rewriting the Eq. (30), for sub-increment:

$$\boldsymbol{r}(\boldsymbol{\sigma}^i, \boldsymbol{q}^i, \Delta\lambda^i) = \begin{cases} \boldsymbol{\sigma}^i - (\boldsymbol{\sigma}^{trial})^i + \Delta\lambda^i \boldsymbol{K}\boldsymbol{m}^i = 0, \\ \boldsymbol{q}^i - \boldsymbol{q}^{i-1} + \Delta\lambda^i \boldsymbol{\varpi}^i = 0, \\ F(\boldsymbol{\sigma}^i, \boldsymbol{q}^i) = 0. \end{cases} \quad (39)$$

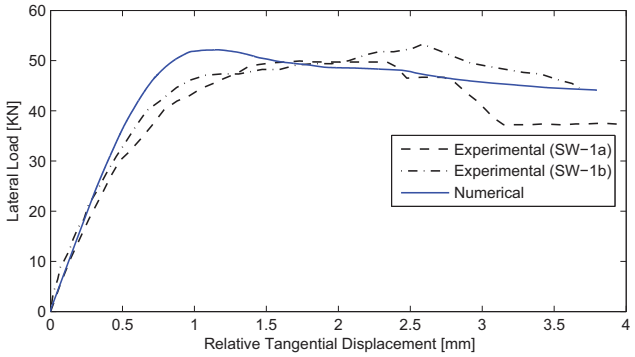

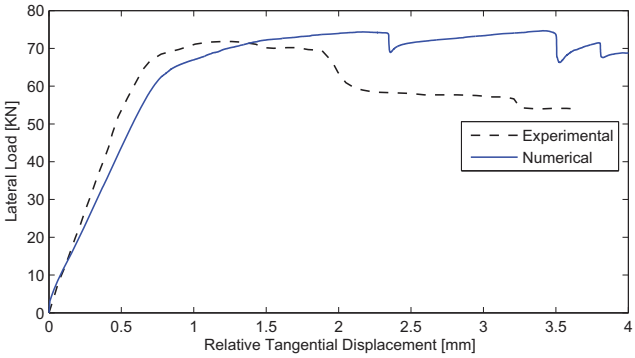

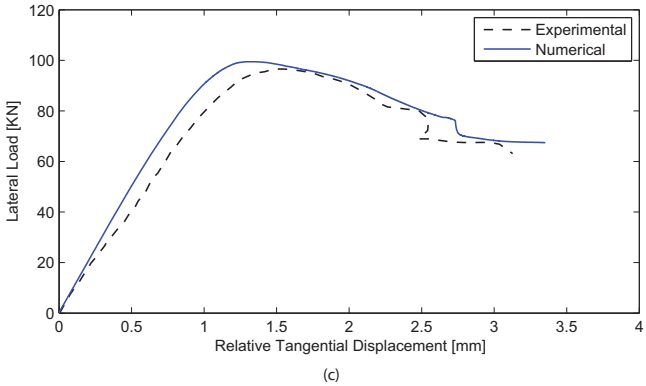

Fig. 8. Comparison of experimental and numerical result obtained from the proposed model: (a) SW-1; (b) SW-2; (c) SW-3.

Note that now the independent variable of the system of equation are $\boldsymbol{\sigma}^i$, $\boldsymbol{q}^i$, $\Delta\lambda^i$ and the methodology for solving the equation is the same as the one in the previous section. For consistent tangent operator we take the derivative of the last converged Jacobian for sub stepping with respect to $\Delta\boldsymbol{\epsilon}$ and then apply the chain rule:

$$\begin{bmatrix} \left[\frac{\partial \boldsymbol{\sigma}^i}{\partial \boldsymbol{\epsilon}^i}\right]_{2x2} \\ \left[\frac{\partial \boldsymbol{q}^i}{\partial \boldsymbol{\epsilon}^i}\right]_{6x2} \\ \left[\frac{\partial \lambda^i}{\partial \boldsymbol{\epsilon}^i}\right]_{1x2} \end{bmatrix}_{9x2} = \boldsymbol{J}^{-1}(\boldsymbol{\sigma}^i_{n+1}, \boldsymbol{q}^i_{n+1}, \Delta\lambda^i_{n+1})_{9x9} \begin{bmatrix} \eta^i \boldsymbol{K} \\ 0 \\ 0 \end{bmatrix}_{9x2} \quad (40)$$

The consistent tangent operator of a sub-increment can be extracted from the preceding expression. The consistent tangent operator of the load step is obtained by linear combination of all the sub-increments and can be written as:

$$\left[\frac{\partial \boldsymbol{\sigma}}{\partial \boldsymbol{\epsilon}}\right] = \sum_{i=0}^{N} \left[\frac{\partial \boldsymbol{\sigma}^i}{\partial \boldsymbol{\epsilon}^i}\right]. \quad (41)$$

6. Numerical Examples

In the present section, a proposed cohesive zone model is applied to the failure analysis of unreinforced masonry for validation, by comparing the numerical results with experimental results available in the literature. The simplified micro modeling is adopted for numerical modeling of unreinforced masonry under plain stress condition. In simplified micro modeling, mortar and a two unit-mortar interface is lumped into the joint between expended units (see Figure 7). The units are expended in order to keep the structure geometry unchanged. Thus, masonry is considered as a set of elastic blocks bonded by potential crack, potential slip, and crushing plane at the joints. The joint interface is modeled with the proposed cohesive zone model.

6.1. *Masonry Shear Wall*

An experimental study was carried out on masonry shear walls by Vermeltfoort and Raijmakers [42, 43]. The authors conducted the tests on two types of shear wall, i.e., one without

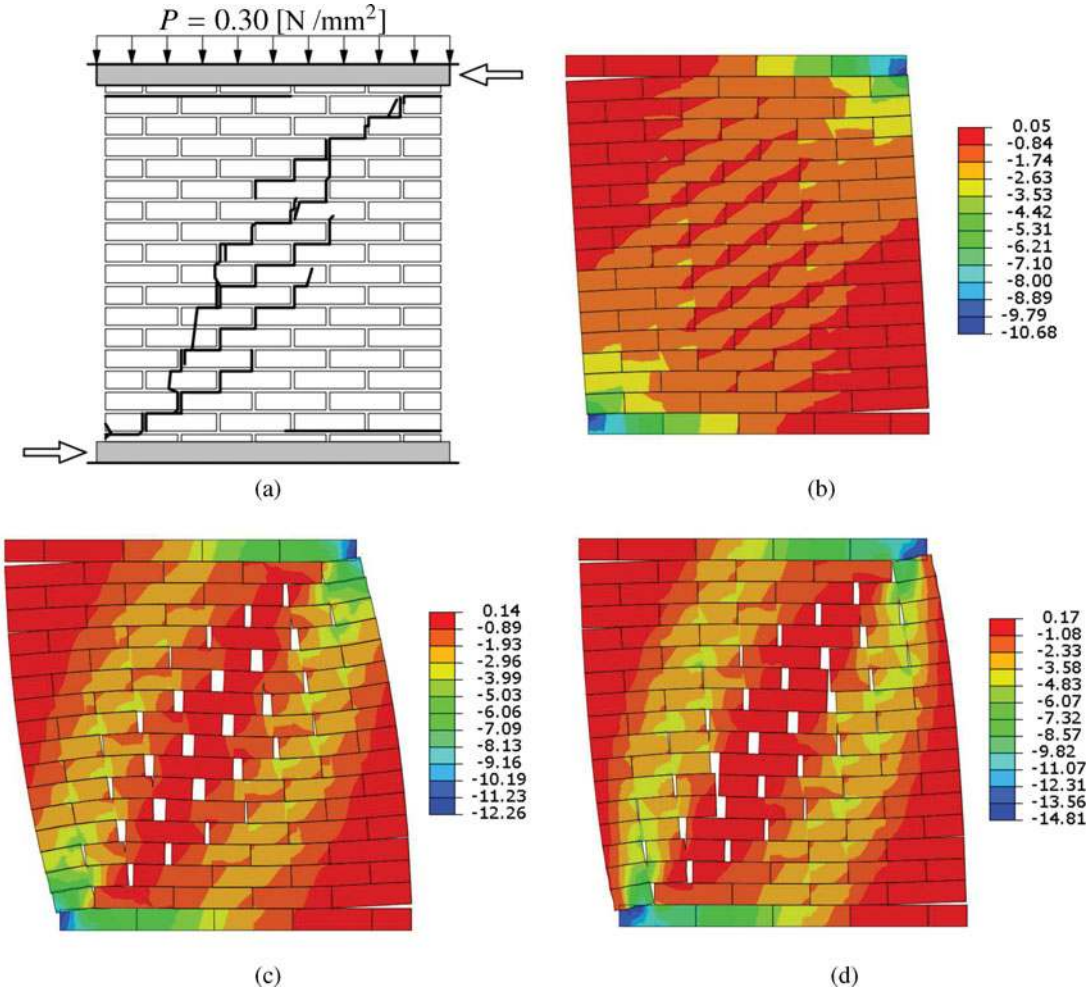

Fig. 9. (a) Experimental failure pattern for shear wall without opening SW-1; minimum principal stress at different displacement with deformed mesh for different shear wall without opening SW-1: (b) $d = 1$ (mm); (c) d = 2 (mm); (d) $d = 4$ (mm).

the opening (SW) and the other with the opening (SWO). The authors used a set-up that consisted of a pier with a width to height ratio of one (dimensions 990 × 1000 [mm^2]). It was built-up with 18 courses, of which two courses were clamped in steel beam and only 16 courses were active. The wall was made up of wire cut solid clay [210 × 52 × 100 mm^3] and mortar [10 mm], prepared with a volumetric cement:lime:sand ratio (1:2:9). The test involves a monotonically increasing horizontal load under different levels of uniformly distributed normal stress, keeping the bottom and top boundaries horizontally fixed.

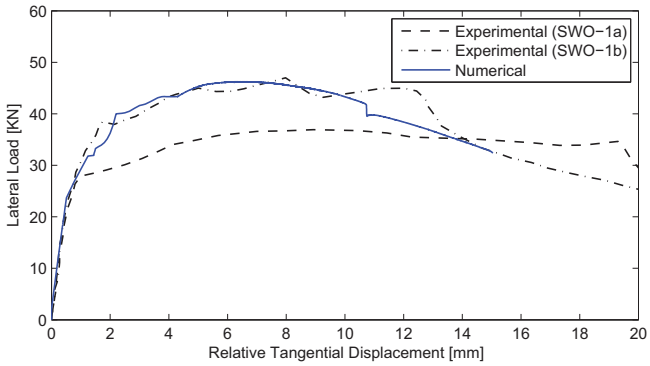

Fig. 10. Comparison of experimental and numerical result obtained from the proposed model for SWO-1.

In the present work, both types of walls are considered for numerical modeling. The micro-properties of the shear wall material are obtained from [42, 43] and are given in Tables 8, 9, and 10. The hardening/softening law for the compression cap is defined by the set $\{\zeta, w_4^p\} = \{(\zeta_p/3, 0.0);\ (\zeta_p, 0.09);\ (\zeta_p/2, 0.49);\ (\zeta_p/7, \infty)\}$. For the numerical analyses, units are represented by plane stress continuum elements (8-noded) while line interface elements (4-noded, with two integration points) are adopted for the joints and for the potential vertical cracks in the middle of the unit.

6.1.1. *Shear Wall Without Opening (SW)*

This wall was considered to be subjected to three different initial vertical pressures, i.e., for the wall SW-1a and SW-1b pressure equals 0.30 [N/mm^2], for the wall SW-2 pressure

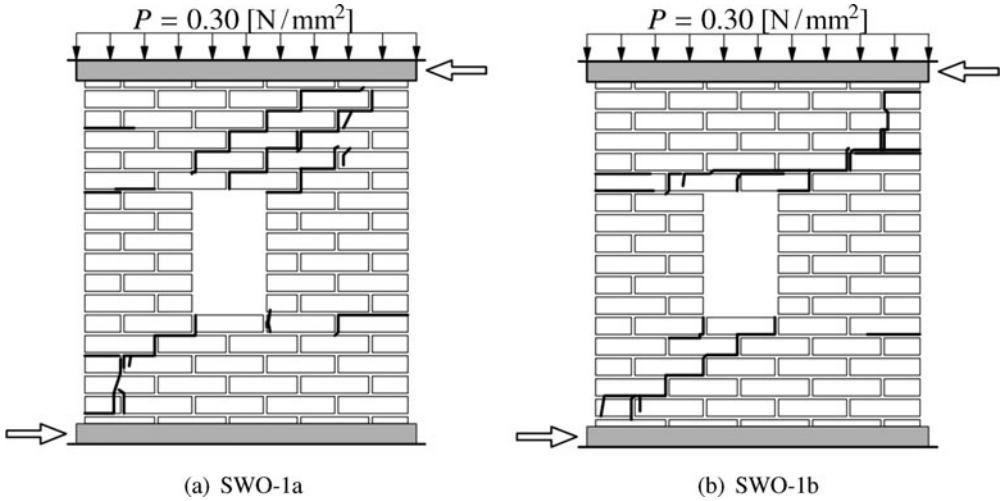

Fig. 11. Experimental failure pattern for the different walls with opening [42, 43, 44] for SWO-1.

equals 1.21 [N/mm^2], and for the wall SW-3 pressure equals 2.12 [N/mm^2]. On application of the monotonically increasing horizontal load, initially horizontal tensile cracks develop at the bottom and top of the wall particularly in the bed joint at an early loading stage and then a diagonal stepped crack form. Finally, the diagonal stepped crack and crushing of the toes of the masonry leads to the overall failure of the masonry, simultaneously causing the bricks to crack.

The comparison between numerical and experimental load-displacement behavior is shown in Figure 8. The experimental behavior is satisfactorily reproduced by the proposed cohesive zone model. All the walls behave in the same manner, confirming the idea that the masonry can withstand substantial post-peak deformation at reduced strength. The masonry shear wall also shows that higher initial vertical loads lead to increase its strength, however ductility deceases.

The sharp load drops in Figure 8b are attributed to sudden drop of shear stress at single integration point of the potential crack, caused by the cracking of a brick. The choice of setting the shear stress in potential crack of brick equal to zero upon initiation of the crack, causes the problems related to convergence, thereby forcing the choice of load steps to be extremely small and impractical. This affects the numerical robustness of the model, due release of a large amount of energy in a single load step. However, if sufficiently fine meshes are adopted, the solution obtained is independent of the size of the load increments. The problem of a large amount of energy release in a single load step is overcome by gradually decreasing the shear stress to zero in several load steps rather than a sudden drop to zero. This assumption allows us to overcome the problem and is confirmed by the numerical example on the shear wall SW-1 and SW-3 (Figures 8a and 8c).

The numerical crack pattern and the minimum principle stress distribution for SW-1 are presented in Figure 9. Initially, the vertical loads are applied, which make the stress distribution continuous. At the early stage of horizontal displacement, small diagonal compression struts form. These struts are defined by the center of the bricks due to the different stiffnesses of joints and bricks (Figure 9b). On further loading, a diagonal stepped crack opens and prevents the formation of compressive struts parallel to the diagonal line defined by the center of the bricks (Figure 9c). Simultaneously, diagonal struts initiate

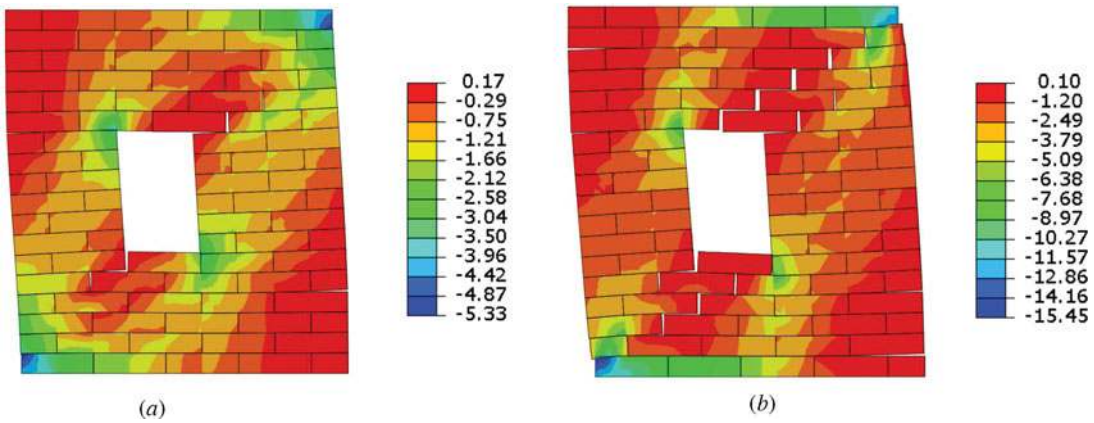

Fig. 12. Minimum principal stress at different displacement (d) with deformed mesh for shear wall with opening for SWO-1: (a) $d = 5$ (mm); (b) $d = 5$ (mm).

the splitting of the bricks due to Possion's effect. When the diagonal cracks are fully open, two distinct struts are formed, one at each side of the diagonal crack. Finally the diagonal stepped crack and crushing of the toes in compression leads to collapse of the shear wall, simultaneously with cracks in the brick (Figure 9d).

6.1.2. *Shear Wall With Opening (SWO)*

These walls are subjected to only normal pressure of 0.30 [N/mm^2]. In these shear walls, opening creates two small weak piers on either side of the opening. Thus, two compressive struts develop under horizontal loading, spreading the load around both sides of the opening. On applying the monotonically increasing horizontal load, first the diagonal zigzag cracks arise from two corners of the opening. Then, the tensile cracks arise from the boundary of the wall at the base and top of the small piers (in the bed joint). Finally, a collapse mechanism is formed by failure of the compressed toes, located at the bottom and top of the wall as well as the small piers.

The comparison between numerical and experimental load-displacement curves are shown in Figure 10. The numerical results are in good agreement with those obtained from the experiments [44]. A good comparison of the SWO-1a and numerical model is obtained because calculated stiffness of the numerical model matches with the experimental values. This indicates that the proposed model is able to predict correct failure mechanism.

The numerical crack pattern and minimum principle stress distribution are presented in the Figure 12. During the initial horizontal loading, two diagonal cracks arise from the corners of the opening. Simultaneously, horizontal cracks in the top and the bottom of the piers also arise (Figure 12a). The load is transferred by the two large compression struts on either side of the opening. On further loading, the previous diagonal crack will stop and two additional diagonal cracks start to open (Figure 12b). The two compression struts become narrower. Finally, the diagonal crack progresses toward the supports and then the compression toes at the top and bottom are crushed. A complete collapse mechanism is formed with the failure of the smaller piers.

7. Discussion and Conclusions

A cohesive zone model interface element has been developed for quasi-brittle materials like masonry by using mathematical theory of plasticity. The proposed model is represented by a single surface yield criteria, which is capable of representing Coulomb friction failure, cracking of material by cut-off and crushing of plain by cap-off in compression. The proposed yield function is simple extension of Mohr–Coulomb criterion, which makes use of property of arc-tan for cut and cap-off. The algorithms have been developed by integrating the differential equations by fully implicit Backward Euler method. These equations are solved by full Newton–Raphson technique in monolithic manner, which leads to combined local and global approach.

A careful and detailed investigation has been performed to check robustness and accuracy of the algorithm for different load paths and nonassociativity. It has been found that sub stepping is required to ensure convergence and accuracy of the final solution at both local and global level. Hence the algorithm is combined with a sub stepping strategy. Finally, validation of the cohesive zone model has been carried out against the experiments carried out on the shear walls. The numerical result shows that the model is able to reproduce the complete path of the structures up to and beyond the peak, until total degradation of strength, without any numerical difficulties in the proposed cohesive zone model.

References

[1] D. Dugdale, Yielding of steel sheets containing slits, J. Mech. Phys. Solids, vol. 8, no. 2, pp. 100–104, 1960.

[2] G. Barenblatt, The mathematical theory of equilibrium cracks in brittle fracture, Adv. Appl. Mech., vol. 7, pp. 55–129, 1962.

[3] J.C. Schellekens and R.D. Borst, On the numerical integration of the interface elements, Int. J. Numer. Methods Eng., vol. 36, pp. 43–66, 1993.

[4] H. Seong, G. Paulino, and G. William, Simulation of crack propagation in asphalt concrete using an intrinsic cohesive zone model, J. Eng. Mech., vol. 11, no. 1322, pp. 1215–1223, 2006.

[5] R.E. Goodman, R.L. Taylor, and T.L. Brekke, A model for the mechanics of jointed rock, J. Soil Mech. Found. Div., vol. 94, no. 3, pp. 637–660, 1968.

[6] I. Carol, A. Gens, and E. Alonso, A three dimensional elastoplastic joint element. Centek Publishers, Lulea, Sweden, 1985.

[7] A. Hillerborg, M. Modéer, and P.-E. Petersson, Analysis of crack formation and crack growth in concrete by means of fracture mechanics and finite elements, Cem. Concr. Res., vol. 6, no. 6, pp. 773–781, 1976.

[8] J.G. Rots, Computational modeling of concrete fracture. PhD thesis, Technische Hogeschool Delft, Delft, Netherlands, 1988.

[9] V. García-Álvarez, R. Gettu, and I. Carol, Numerical analysis of mixed mode fracture in concrete using interface elements, In: E. Oñate et al. (Eds.), European Congress on Computational Methods in Applied Sciences and Engineering – ECCOMAS 2000, CIMNE, September 11–14, Barcelona, Spain, 2000. (CD-ROM).

[10] D. Garolera, C. López, I. Carol, and P. Papanastasiou, Micromechanical analysis of the rock sanding problem, J. Mech. Behav. Biomed. Mater., vol. 16, no. 1–2, pp. 45–54, 2005.

[11] T. Bittencourt, A. Ingraffea, and J. Llorca, Simulation of arbitrary, cohesive crack propagation, Fract. Mech. Concr. Struct., vol. 1, pp. 339–350, 1992.

[12] M. Ortiz and A. Pandolfi, Finite-deformation irreversible cohesive elements for three-dimensional crack-propagation analysis, Int. J. Numer. Methods Eng., vol. 44, no. 9, pp. 1267–1282, 1999.

[13] J. Ghaboussi, E.L. Wilson, and J. Isenberg, Finite element for rock joints and interfaces, J. Soil Mech. Found. Div., vol. 99, no. 10, pp. 849–862, 1973.

[14] C. Desai, M. Zaman, J. Lightner, and H. Siriwardane, Thin-layer element for interfaces and joints, Int. J. Numer. Anal. Meth. Geomech., vol. 8, no. 1, pp. 19–43, 1984.

[15] A. Gens, I. Carol, and E. Alonso, An interface element formulation for the analysis of soil-reinforcement interaction, Comput. Geotech., vol. 7, no. 1, pp. 133–151, 1989.

[16] A. Page, Finite element model for masonry, J. Struct. Div., vol. 104, no. 8, pp. 1267–1285, 1978.

[17] T. Stankowski, Numerical simulation of progressive failure in particle composites, Ph.D. Thesis, Technical. University of Colorado, Boulder, Colorado, 1990.

[18] T. Stankowski, K. Runesson, and S. Sture, Fracture and slip of interfaces in cementitious composites, I: Characteristics, J. Eng. Mech., vol. 119, no. 2, pp. 292–314, 1993.

[19] J.G. Rots, W.G. Berkers, and H.V.D. Heuvel, Towards fracture mechanics based design rules for movement-joint spacing, Proceedings of the 10th International Brick and Block Masonry Conference, pp. 707–717, July 5–7, Calgary, Alberta, Canada, 1994.
[20] H.R. Lotfi and P.B. Shing, Interface model applied to fracture of masonry structures, J. Struct. Eng., vol. 120, no. 1, pp. 63–80, 1994.
[21] P.B. Lourenço and J.G. Rots, Multisurface interface model for analysis of masonry structures, J. Eng. Mech., vol. 123, no. 7, pp. 660–668, 1997.
[22] X.-P. Xu and A. Needleman, Numerical simulations of fast crack growth in brittle solids, J. Mech. Phys. Solids, vol. 42, no. 9, pp. 1397–1434, 1994.
[23] G. Camacho and M. Ortiz, Computational modelling of impact damage in brittle materials, Int. J. Solids Struct., vol. 33, no. 20, pp. 2899–2938, 1996.
[24] K. Willam, I. Rhee, and B. Shing, Interface damage model for thermomechanical degradation of heterogeneous materials, Comput. Meth. Appl. Mech. Eng., vol. 193, no. 30, pp. 3327–3350, 2004.
[25] A. Caballero, I. Carol, and C. López, A meso-level approach to the 3D numerical analysis of cracking and fracture of concrete materials, Fatigue Fract. Eng. Mater. Struct., vol. 29, no. 12, pp. 979–991, 2006.
[26] M.E. Plesha, R. Ballarini, and A. Parulekar, Constitutive model and finite element procedure for dilatant contact problems, J. Eng. Mech., vol. 115, no. 12, pp. 2649–2668, 1989.
[27] T. Stankowski, K. Runesson, and S. Sture, Fracture and slip of interfaces in cementitious composites, I: Characteristics, J. Eng. Mech., vol. 119, no. 2, pp. 292–314, 1993.
[28] T. Stankowski, K. Runesson, and S. Sture, Fracture and slip of interfaces in cementitious composites, II: Implementation, J. Eng. Mech., vol. 119, no. 2, pp. 315–327, 1993.
[29] K.D. Papoulia, C.-H. Sam, and S.A. Vavasis, Time continuity in cohesive finite element modeling, Int. J. Numer. Methods Eng., vol. 58, no. 5, pp. 679–701, 2003.
[30] C.-H. Sam, K.D. Papoulia, and S.A. Vavasis, Obtaining initially rigid cohesive finite element models that are temporally convergent, Eng. Fract. Mech., vol. 72, no. 14, pp. 2247–2267, 2005.
[31] R. Van der Pluijm, H. Rutten, and M. Ceelen, Shear behaviour of bed joints, Proceedings of the 12th International Brick/Block Masonry Conference, pp. 1849–1862, June 25–28, Madrid, Spain, 2000.
[32] R. Atkinson, B. Amadei, S. Saeb, and S. Sture, Response of masonry bed joints in direct shear, J. Struct. Eng., vol. 115, no. 9, pp. 2276–2296, 1989.
[33] R. van der Pluijm, Shear behaviour of bed joints, Proceedings of the 6th North American Masonry Conference, June 6–9, Philadelphia, Pennsylvania, 1993.
[34] G.N. Pande, G.G. Beer, and J.R. Williams, Numerical Methods in Rock Mechanics, G.N. Pande, G. Beer, and J.R. Williams, Eds., Wiley, Chichester, New York, 1990.
[35] J. Simo and T. Hughes, Computational Inelasticity, Springer, New York, 1998.
[36] O.C. Zienkiewicz, R.L. Taylor, and J.Z. Zhu, The Finite Element Method: Its Basis and Fundamentals (Vol. 1), Butterworth-Heinemann, Oxford, UK, 2005.
[37] S.O. Niels and R. Matti, The Mechanics of Constitutive Modeling, Elsevier Ltd., Oxford, UK, 2005.
[38] V. ABAQUS, 6.9 Online Documentation, SIMULIA Inc.
[39] A. Pérez-Foguet, A. Rodrıguez-Ferran, and A. Huerta, Consistent tangent matrices for substepping schemes, Comput. Meth. Appl. Mech. Eng., vol. 190, no. 35, pp. 4627–4647, 2001.
[40] W. Wang, M. Datcheva, T. Schanz, and O. Kolditz, A sub-stepping approach for elasto-plasticity with rotational hardening, Comput. Mech., vol. 37, no. 3, pp. 266–278, 2006.
[41] A. Caballero, K. Willam, and I. Carol, Consistent tangent formulation for 3d interface modeling of cracking/fracture in quasi-brittle materials, Comput. Meth. Appl. Mech. Eng., vol. 197, no. 33, pp. 2804–2822, 2008.
[42] T. Raijmakers and A.T. Vermeltfoort, Deformation controlled tests in masonry shear walls, Report B-92-1156, TNO BouW, Delft, The Netherlands, 1992.
[43] A.T. Vermeltfoort and T. Raijmakers, Deformation controlled tests in masonry shear walls, Part 2, Technical Report TUE/BKO/93.08, Eindhoven University of Technology, Eindhoven, Netherlands, 1993.
[44] P. Lourenço, Computational Strategies for Masonry Structures, Delft University Press, Delft, Netherlands, 1996.

Appendix A: Expression of Cohesive Model, First and Second Derivatives

$$T_1 := [(C - \sigma_{nn}\tan(\phi))], \quad T_2 := [C_Q - \sigma_{nn}\tan(\psi)],$$

$$f_t(\boldsymbol{\sigma}, \boldsymbol{q}) := \frac{2}{\pi}\arctan\left(\frac{\xi - \sigma_{nn}}{\alpha_t}\right), \quad D_t := 1 + \left(\frac{\sigma_{nn} - \xi}{\alpha_t}\right)^2,$$

$$f_c(\boldsymbol{\sigma}, \boldsymbol{q}) := \frac{2}{\pi}\arctan\left(\frac{\sigma_{nn} - \zeta}{\alpha_c}\right), \quad D_c := 1 + \left(\frac{\sigma_{nn} - \zeta}{\alpha_t}\right)^2,$$

$$F(\boldsymbol{\sigma}, \boldsymbol{q}) := -[(C - \sigma_{nn}\tan(\phi))]^2 f_c f_t + \sigma_{tt}^2,$$

$$Q(\boldsymbol{\sigma}, \boldsymbol{q}) := -[C_Q - \sigma_{nn}\tan(\psi)]^2 f_c f_t + \sigma_{tt}^2,$$

$$\boldsymbol{n} = \left[2T_1\tan\phi f_c f_t - T_1^2\left(\frac{2f_c}{\pi\alpha_t D_t} + \frac{2f_t}{\pi\alpha_c D_c}\right)2\sigma_{tt}\right],$$

$$\boldsymbol{m} = \left[2T_2\tan\psi\, f_c f_t - T_2^2\left(\frac{2f_c}{\pi\alpha_t D_t} + \frac{2f_t}{\pi\alpha_c D_c}\right)2\sigma_{tt}\right].$$

Derivative of $\boldsymbol{m}$:

$$T_3 = \frac{f_c}{\pi\alpha_t^3 D_t^2} + \frac{f_t}{\pi\alpha_c^3 D_c^2} + \frac{4}{\pi^2\alpha_t D_t \alpha_c D_c},$$

$$\frac{\partial \mathbf{m}}{\partial \boldsymbol{\sigma}} = \begin{bmatrix} -2\tan^2\psi\, f_c f_t + 8T_2\tan\psi\left(\frac{f_c}{\pi\alpha_t D_t} + \frac{f_t}{\pi\alpha_c D_c}\right) + 2T_2^2 T_3 & 0 \\ 0 & 2 \end{bmatrix},$$

$$\frac{\partial m_1}{\partial \boldsymbol{q}} = \begin{bmatrix} 0 \\ 2\tan\psi\, f_c f_t - 4T_2\left(\frac{f_c}{\pi\alpha_t D_t} + \frac{f_t}{\pi\alpha_c D_c}\right) \\ 0 \\ 2\sec^2\psi\, f_c f_t (T_2 - \sigma_{nn}\tan\psi) \\ -2(\sigma_{nn}\sec^2\psi - 2T_2)\left(\frac{f_c}{\pi\alpha_t D_c} + \frac{f_t}{\pi\alpha_c D_c}\right) \\ \frac{-4\tan\psi\, T_2 f_c}{\pi\alpha_t D_t} + 4T_2\left(\frac{1}{\pi^2\alpha_c D_c \alpha_t D_t} - \frac{f_c(\sigma - \xi)}{\pi\alpha_t^3 D_t^2}\right) \\ \frac{-4\tan\psi\, T_2 f_t}{\pi\alpha_c D_c} + 4T_2\left(\frac{1}{\pi^2\alpha_c D_c \alpha_t D_t} - \frac{f_c(\sigma - \xi)}{\pi\alpha_c^3 D_c^2}\right) \end{bmatrix},$$

$$\boldsymbol{H} = \begin{bmatrix} \langle \sigma_{nn} \rangle & 0 \\ 0 & \sigma_{tt} - \sigma_{t_{r1}} sign(\sigma_{tt}) \\ 0 & (\sigma_{tt_{r1}} - \sigma_{tt_{r2}}) sign(\sigma_{tt}) \\ \langle\langle \sigma_{nn} \rangle\rangle & 0 \end{bmatrix},$$

$$\boldsymbol{\varpi} = \begin{bmatrix} \left(-m_1 \boldsymbol{H}(1,1)\dfrac{\beta_C}{G_f^I} - m_2 \boldsymbol{H}(2,2)\dfrac{\beta_C}{G_f^{II}}\right) \\ \qquad -\beta_C \left(\dfrac{w_1^p}{G_f^I} + \dfrac{w_2^p}{G_f^{II}}\right) \\ \qquad (C_0 - C_r)\exp \\ \left(-m_1 \boldsymbol{H}(1,1)\dfrac{\beta_{C_Q}}{G_f^I} - m_2 \boldsymbol{H}(2,2)\dfrac{\beta_{C_Q}}{G_f^{II}}\right) \\ \qquad -\beta_{C_Q} \left(\dfrac{w_1^p}{G_f^I} + \dfrac{w_2^p}{G_f^{II}}\right) \\ \qquad (C_{Q_0} - C_{Q_r})\exp \\ -m_2 \boldsymbol{H}(3,2)\beta_\phi(\phi_0 - \phi_r)\exp^{-\beta_\phi w_3^p} \\ -m_2 \boldsymbol{H}(3,2)\beta_\psi(\psi_0 - \psi_r)\exp^{-\beta_\psi w_3^p} \\ \left(-m_1 \boldsymbol{H}(1,1)\dfrac{\beta_\xi}{G_f^I} - m_2 \boldsymbol{H}(2,2)\dfrac{\beta_\xi}{G_f^{II}}\right) \\ \qquad -\beta_\xi \left(\dfrac{w_1^p}{G_f^I} + \dfrac{w_2^p}{G_f^{II}}\right) \\ \qquad \xi_0 \exp \\ -m_1 \boldsymbol{H}(4,1)\dfrac{\partial \zeta}{\partial w_4} \end{bmatrix},$$

$$\frac{\partial \zeta}{\partial w_4} = \begin{cases} 2(\zeta_p - \zeta_0)\left(\left(\dfrac{2w_4^p}{w_p}\right) - \left(\dfrac{w_4^p}{w_p}\right)^2\right)^{-\frac{1}{2}} & \\ \quad \left(\dfrac{2}{w_p} + \dfrac{2w_4}{w_p^2}\right) & \text{if } w_4^p \le w_p \\ 2(\zeta_m - \zeta_p)\left(\dfrac{w_4^p - w_p}{(w_m - w_p)^2}\right) & \text{if } w_p \le w_4^p \le w_m \\ \beta_\zeta \exp^{\beta_\zeta \left(\frac{w_4^p - w_p}{\zeta_m - \zeta_r}\right)} & \text{if } w_4^p > w_m \end{cases}.$$

Appendix B: Algorithms for Local Newton Solvers

Steps

1. Recover Solution Dependent Variables from the last converged iteration cycle

$$\boldsymbol{\sigma}_{n+1}, \boldsymbol{q}_n, \boldsymbol{W}_n^p, \boldsymbol{\epsilon}_n^p$$

2. Compute trial elastic stress

$$\boldsymbol{\sigma}_{n+1}^{trial} = \boldsymbol{\sigma}_n + \boldsymbol{K}\Delta\boldsymbol{\epsilon}$$

3. Compute the yield function $F^{trial}(\boldsymbol{\sigma}_{n+1}^{trial}, \boldsymbol{q}_n)$

4. Check for the yield condition

if $F^{trial}(\boldsymbol{\sigma}_{n+1}^{trial}, \boldsymbol{q}_n) < 0$ then

Elastic State

update $\boldsymbol{\sigma}_{n+1} = \boldsymbol{\sigma}_{n+1}^{trial}$;

update $\boldsymbol{q}_{n+1} = \boldsymbol{q}_n$;

update $\boldsymbol{W}_n^p = \boldsymbol{W}_n^p$;

update $\boldsymbol{\epsilon}_n^p = \boldsymbol{\epsilon}_n^p$;

else

Plastic State

Compute the contact point $F(\boldsymbol{\sigma}_n + \gamma\Delta\boldsymbol{\sigma}, \boldsymbol{q}_n)$;

While$||\boldsymbol{r}(\boldsymbol{\sigma}_n, \boldsymbol{q}_n, \Delta\lambda_n)|| < tol$

Compute $\boldsymbol{n}_n^k, \boldsymbol{m}_n^k, \boldsymbol{\varpi}_n^k$;

Compute $\boldsymbol{J}_n^k(\boldsymbol{\sigma}_n^k, \boldsymbol{q}_n^k, \Delta\lambda_n^k) = \dfrac{\boldsymbol{r}(\boldsymbol{\sigma}_n^k, \boldsymbol{q}_n^k, \Delta\lambda_n^k)}{\partial(\boldsymbol{\sigma}_n^k, \boldsymbol{q}_n^k, \lambda_n^k)}$;

Compute $\delta(\boldsymbol{\sigma}_n, \boldsymbol{q}_n, \lambda_n)^{k+1} = -\boldsymbol{J}^{-1}(\boldsymbol{\sigma}_n^k, \boldsymbol{q}_n^k, \Delta\lambda_n^k)$ $\mathrm{r}(\boldsymbol{\sigma}_n^k, \boldsymbol{q}_n^k, \Delta\lambda_n^k)$;

Compute $[\boldsymbol{\sigma}_n, \boldsymbol{q}_n, \lambda_n]^{k+1} = [\boldsymbol{\sigma}_n, \boldsymbol{q}_n, \lambda_n]^k + \delta(\boldsymbol{\sigma}_n, \boldsymbol{q}_n, \lambda_n)^{k+1}$;

end

update $\boldsymbol{\sigma}_{n+1} = \boldsymbol{\sigma}_n^{k+1}$;

update $\boldsymbol{q}_{n+1} = \boldsymbol{q}_n^{k+1}$;

update $\boldsymbol{W}_{n+1}^p = (\boldsymbol{W}_n^p)^{k+1}$;

update $\boldsymbol{\epsilon}_n^p = (\boldsymbol{\epsilon}_n^p)^{k+1}$;

Compute $\boldsymbol{K}^{ep}$

end

Algorithm 1: Monolithic numerical integration algorithm.

Steps

1. Recover Solution Dependent Variables from the last converged iteration cycle

$$\boldsymbol{\sigma}_{n+1}, \boldsymbol{q}_n, \boldsymbol{W}_n^p, \boldsymbol{\epsilon}_n^p$$

2. Compute trial elastic stress

$$\boldsymbol{\sigma}_{n+1}^{trial} = \boldsymbol{\sigma}_n + \boldsymbol{K}\Delta\boldsymbol{\epsilon}$$

3. Compute the yield function $F^{trial}(\boldsymbol{\sigma}_{n+1}^{trial}, \boldsymbol{q}_n)$

4. Check for the yield condition

if $F^{trial}(\boldsymbol{\sigma}_{n+1}^{trial}, \boldsymbol{q}_n) < 0$ **then**

Elastic State

update $\boldsymbol{\sigma}_{n+1} = \boldsymbol{\sigma}_{n+1}^{trial}$;

update $\boldsymbol{q}_{n+1} = \boldsymbol{q}_n$;

update $\boldsymbol{W}_n^p = \boldsymbol{W}_n^p$;

update $\boldsymbol{\epsilon}_n^p = \boldsymbol{\epsilon}_n^p$;

else

Plastic State

Compute the contact point $F(\boldsymbol{\sigma}_n + \gamma\Delta\boldsymbol{\sigma}, \boldsymbol{q}_n)$;

Compute $(\boldsymbol{K}^{ep})^0 = \gamma\boldsymbol{K}$;

While $i < n$

While $||\boldsymbol{r}(\boldsymbol{\sigma}_n, \boldsymbol{q}_n, \Delta\lambda_n)|| < tol$ **do**

for simplicity superscript 'i' is not used ;

Compute $\boldsymbol{n}_n^k, \boldsymbol{m}_n^k, \boldsymbol{\varpi}_n^k$;

Compute $\boldsymbol{J}_n^k(\boldsymbol{\sigma}_n^k, \boldsymbol{q}_n^k, \Delta\lambda_n^k) = \dfrac{\boldsymbol{r}(\boldsymbol{\sigma}_n^k, \boldsymbol{q}_n^k, \Delta\lambda_n^k)}{\partial(\boldsymbol{\sigma}_n^k, \boldsymbol{q}_n^k, \lambda_n^k)}$;

Compute $\delta(\boldsymbol{\sigma}_n, \boldsymbol{q}_n, \lambda_n)^{k+1} = -\boldsymbol{J}^{-1}$
$(\boldsymbol{\sigma}_n^k, \boldsymbol{q}_n^k, \Delta\lambda_n^k)\mathrm{r}(\boldsymbol{\sigma}_n^k, \boldsymbol{q}_n^k, \Delta\lambda_n^k)$;
Compute $[\boldsymbol{\sigma}_n, \boldsymbol{q}_n, \lambda_n]^{k+1}$
$= [\boldsymbol{\sigma}_n, \boldsymbol{q}_n, \lambda_n]^k \delta(\boldsymbol{\sigma}_n, \boldsymbol{q}_n, \lambda_n)^{k+1}$;
end
update $(\boldsymbol{\sigma}_{n+1})^i = (\boldsymbol{\sigma}_n^{k+1})^i$;
update $(\boldsymbol{q}_{n+1})^i = (\boldsymbol{q}_n^{k+1})^i$;
update $(\boldsymbol{W}_{n+1}^p)^i = ((\boldsymbol{W}_n^p)^{k+1})^i$;
Compute $(\boldsymbol{K}^{ep})^i$
end
update $\boldsymbol{\sigma}_{n+1} = (\boldsymbol{\sigma}_n^{k+1})^N$;
update $\boldsymbol{q}_{n+1} = (\boldsymbol{q}_n^{k+1})^N$;
update $\boldsymbol{W}_{n+1}^p = ((\boldsymbol{W}_n^p)^{k+1})^N$;
Compute $\boldsymbol{K}^{ep} = \sum_{i=0}^{N} (\boldsymbol{K}^{ep})^i$
end

Algorithm 2: Monolithic numerical integration algorithm with sub-stepping.